Identification of reaction rate parameters from uncertain spatially distributed concentration data using gradient-based PDE constrained optimization

Shota Ito [a,b,*], Julius Jeßberger [a,c], Stephan Simonis [a,c], Fedor Bukreev [a,b], Adrian Kummerländer [a,c], Alexander Zimmermann [d], Gudrun Thäter [c], Georg R. Pesch [e], Jorg Thöming [d], Mathias J. Krause [a,b,c]

[a] *Lattice Boltzmann Research Group, Karlsruhe Institute of Technology, Karlsruhe, Germany*
[b] *Institute of Mechanical Process Engineering and Mechanics, Karlsruhe Institute of Technology, Karlsruhe, Germany*
[c] *Institute for Applied and Numerical Mathematics, Karlsruhe Institute of Technology, Karlsruhe, Germany*
[d] *Center for Environmental Research and Sustainable Technology, University of Bremen, Bremen, Germany*
[e] *School of Chemical and Bioprocess Engineering, University College Dublin, Dublin, Ireland*

ARTICLE INFO

ABSTRACT

A promising approach to quantify reaction rate parameters is to formulate and solve inverse problems by minimizing the deviation between simulation and measurement. One major challenge may become the non-uniqueness of the recovered parameters due to the ill-posed problem formulation, which requires sophisticated approaches such as regularization. This study investigates the feasibility of using spatially distributed reference data, i.e., concentration distributions of reactive flows, which could be obtained by magnetic resonance imaging (MRI), instead of isolated points or integral values to recover reaction rate parameters. We propose a combined framework of computational fluid dynamics (CFD) and gradient-based optimization methods, which minimizes the difference between the simulated concentration distribution and a given data set by automatic iterative parameter adjustments. The forward problem is formulated as a coupled system of reaction-advection-diffusion equations (RADE), which is solved by the lattice Boltzmann method (LBM). Therefore, a system of non-linear partial differential equations (PDE) acts as optimization constraints, limiting the possible outcomes of the inverse problem. A benchmark test case using a CFD simulation as reference data confirms the validity of the presented method by successfully identifying up to three *a priori* set reaction parameters reversely. With it, initial relative errors could be reduced from around 150% to 10^{-3}% in 13 optimization steps corresponding to 37 simulations. Even after reducing the accessible reference data from 2D concentration distributions to 1D outflow concentration distribution or by adding noise signals onto the reference data with a signal-to-noise ratio (SNR) of 5, our framework successfully recovered the parameters with a relative error of ≈ 1%. Both, the chosen LBM and optimization algorithms are implemented in the open-source library OpenLB.

1. Introduction

Chemical reactions are omnipresent due to their indispensable role in various industrial processes across numerous applications. Even minute improvements in the reaction process or reactor design can have significant economic and ecological impacts. Generally, achieving this requires properly fitted/adapted models and knowledge of their reaction-specific parameters. Although the basic principles such as the reaction mechanism are often well known, finding appropriate values

that describe the process at practical conditions remains a challenging task [1]. In many cases, for example heterogeneous reactions that take place in a fixed-bed reactor, the overall/macroscopic reaction rate is strongly influenced by the prevailing transport processes [2]. Then, detailed information on the transport phenomena is additionally required to optimize the chemical reaction process.

The reaction rate law contains several parameters, e.g., the reaction constant and reaction orders of the involved species. To determine those parameters for a single chemical reaction, one usually conduct

---

* Corresponding author at: Lattice Boltzmann Research Group, Karlsruhe Institute of Technology, Karlsruhe, Germany.
E-mail address: shota.ito@kit.edu (S. Ito).

numerous experiments and measurements at ideal conditions which usually differs from the actual process conditions [1]. In addition to that, any changes in the underlying transport phenomena of the reactants might also significantly impact the final conversion rate without actually influencing the microscopic rate parameters. Quantifying both microscopic rate parameters as well as parameters describing the transport phenomena is a tedious, challenging, and expensive task involving several experiments as well as requiring expert knowledge [1].

A promising approach for parameter identification is to formulate an inverse problem and solve it by utilizing methods of optimization [3]. The methodology is applied in several fields of engineering, e.g., in identifying material parameters [4–6], in biomedical engineering [7,8], as well as in identifying reaction parameters [9–13]. In the inverse problem, the reaction rate parameters are obtained from the reference data, e.g., experimentally measured data, by minimizing the difference between the experimental and simulated results. Since the numerical model producing the simulation results is fully parameterized, the simulation sufficiently close to the experimental data directly yields the desired reaction rate law parameters.

Reactive flow problems are modeled by conservation equations such as Navier-Stokes equations or reaction-advection-diffusion equations (RADE) for each reaction species coupled with the reaction rate law, which leads to systems of partial differential equations (PDE). The lattice Boltzmann method (LBM) has proven to be a very effective and highly stable method for modeling fluid flow in various applications, e.g., biomedical problems [14,15], turbulent flows [16–19], and transport phenomena governed by advection and diffusion such as reactive flows [20–25]. Its great scalability due to mainly local operations makes the LBM attractive for expensive numerical investigations [26,27].

Inverse problems involving reactive flows contain conservation equations as constraint functions of the optimization problem. As solving this problem with one-shot methods as introduced in [28] is not possible, an iterative scheme becomes necessary requiring to solve the system of conservation equations multiple times. Heuristic optimization methods have advantages such as their global character of search, no computation of gradients, and easy implementation [11]. However, applying heuristic approaches to solve inverse problems would involve performing $\approx \mathcal{O}(10000)$ simulations which is currently too expensive. Gradient-based optimization methods such as, e.g., steepest descent, Newton or quasi-Newton methods like L-BFGS [29], only converge towards an local optimum but they require much fewer optimization steps to converge compared to heuristic approaches. A convex problem formulation is required to ensure that the found optimum is the global optimum in case such gradient-based methods are used, which is generally very difficult or even impossible for complex systems to show. Furthermore, inverse problems, e.g., parameter identification of reaction rate laws with noisy measurement data as input, are generally ill-posed [9,13,30,31]. That is, when the simulation is compared against integral measurements only, such as the averaged product concentration, minimizing the difference between simulation and measurement does generally not have only one unique solution. Thus, the non-uniqueness regarding the possible solutions to the inverse problem makes it a challenging task to reliably identify reaction rate parameters. To counteract this problem, Kügler et al. [9] applied regularization methods by adding penalty terms in the minimizing objective function. Opara et al. [31] utilized combinations of concave loss functions for the objective function with regularization techniques.

Through the rise of more sophisticated measurement techniques such as magnetic resonance imaging (MRI), non-invasive measurements of spatially distributed chemical reactions are now available [32]. The great synergy between CFD and MRI as well as the suitability of spatially distributed measurement data, e.g., obtained by MRI, to solve inverse problems is successfully demonstrated in previous studies by Klemens *et al.* [33–36]. Therein, inverse problems are solved for domain identification and a method for noise reduction of MRI flow measurements is presented [33]. In other applications, the utilization of spatially distributed data in inverse problems also yields good results [6,37]. Inspired by those studies, a promising approach to solve the parameter identification problem in reactive flows could be the utilization of spatially distributed data sets instead of averaged or scalar values as used in other publications attempting to identify reaction rate parameters [13,31,9,30,10]. That is, the optimization problem minimizes the error between a spatially distributed reference concentration field and a CFD simulation of the corresponding reactive flow computed on every grid node of the simulation domain. This restricts the possible outcomes of the optimization problem to those which are solutions of the approximated conservation equations. Huang *et al.* [38] utilized in their work temperature and concentration distributions measured on surfaces in order to estimate the heat and mass production rate distributions in chemically reacting fluids. Therein, they used a 1D model for the transport process, whereas, in the presented work, a CFD simulation is performed, delivering resolved 2D/3D concentration distributions of the reacting flow. The flow simulation with the identified reaction rate parameters automatically contains the minimized difference to measurement data being a preferred outcome of most numerical studies. Using spatial distributions of the reactant concentrations might be a promising approach to reduce the number of possible solutions to the parameter identification problem counteracting the non-uniqueness of the optimization result.

Therefore, this study aims to investigate the feasibility of spatially distributed data for identifying reaction rate parameters in reactive flows. A parameter identification framework is presented, combining L-BFGS with the LBM as a highly scalable discretization scheme of the underlying conservation equations to solve the inverse problem efficiently. For the gradient computations, the forward mode of algorithmic differentiation (AD) and finite difference stencils are used. A benchmark test case validates the presented method for a quasi-2D homogeneous reaction in a bulk flow where a CFD simulation with *a priori* known reaction rate parameters is used as the reference concentration field. The parameter identification framework finds the rate parameters from the simulated reference concentration fields, which are then compared with the initially set parameters. With the benchmark case, we focus our investigations on the accuracy of the recovered parameters, the robustness of the optimization problem, and, briefly, the performance of the parameter identification framework. Striving to apply the presented method to real measurement data in future works, we will test the reduction of the included reference data, i.e., only using the outflow product distribution and investigate uncertainty in form of artificial noise signals imposed onto the reference concentration distributions imitating MRI measurements. To the best of the author's knowledge, this is the first attempt to use spatially distributed concentration data to identify reaction rate parameters in terms of solving inverse problems by using CFD simulations and gradient-based optimization methods. All presented methods and conducted studies are implemented in the open-source library OpenLB [39,40].

This paper is structured as follows: In Sec. 2, the general optimization problem is formulated for the parameter identification problem in reactive flows. This is followed by Sec. 3, where the presented solution strategy is explained in order to solve the parameter identification problem. Then, Sec. 4 introduces the reactive flow problem on which the presented method is applied as the benchmark problem to validate the parameter identification method. Five cases investigate the presented method regarding the mentioned aspects. Finally, Sec. 5 provides a concise summary of the highlights of the present work.

2. Parameter identification in homogeneous reactive flows

This chapter is dedicated to the formulation of the general constraint optimization problem we aim to solve to identify reaction rate parameters from given reference concentration distributions, e.g., obtained by measurements. First, Sec. 2.1 contains the formulation of the optimization problem. Then, Sec. 2.2 specifies the constraint function considered
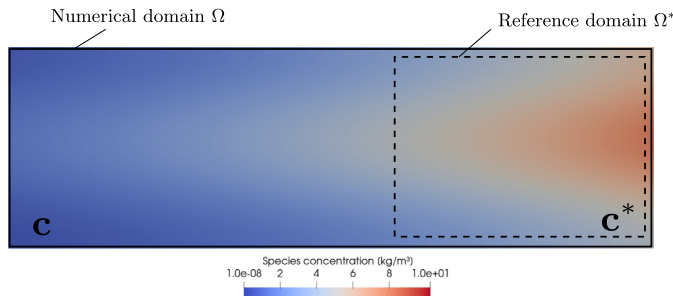
Fig. 1. Inside the dashed domain Ω^*, reference data is assumed to be available, e.g., obtained by MRI measurements. The optimization problem minimizes the deviation between the simulated concentration distribution $\mathbf{c}$ and reference concentration distribution $\mathbf{c}^*$ inside Ω^* to identify the reaction rate parameters.

during optimization. The provided problem formulation here is independent of the applied discretization scheme. The chosen discretization strategy to solve the optimization problem in the presented work is specified in Sec. 3.

2.1. Formulation of the optimization problem

Our general approach to parameter identification is to find a set of model parameters such that the corresponding simulated reaction species concentration distributions are sufficiently close to the corresponding reference concentration distributions, e.g., obtained by measurements. We assume that our numerical model captures the same physics as the reference concentration distributions to ensure that the recovered model parameters correspond to those we aim to identify. The current study considers only stationary reactive flow problems such that the deviation between fully converged simulation and reference distributions is minimized. As we aim to apply the presented method to concentration distributions measured by MRI in the future, the choice to consider stationary flow fields can be beneficial as MRI generally requires a long measurement duration and faces difficulties in capturing rapid changes in the flow and resulting concentration field. Fig. 1 illustrates the presented approach where spatially distributed reference results are utilized to solve the inverse problem of identifying reaction rate parameters. The outer domain indicated by the black solid line contains the fluid domain, where a CFD simulation computes concentration distributions, referred to as the *numerical domain* $\Omega \subseteq \mathbb{R}^d$, with $d \geq 1$ denoting the spatial dimension. Note that Ω is not referring to the discretized numerical domain $\Omega_{\triangle x} \subseteq \Omega$ (further specified in Sec. 3). The area in the figure indicated by the dashed lines depicts the *reference domain* $\Omega^* \subseteq \Omega$ where reference data on the concentration distributions are available, e.g., the area containing the obtained measurement data. In practice, the spatial positions of grid points in the CFD simulation $\mathbf{x} \in \Omega_{\triangle x}$ and the positions $\mathbf{x}^* \in \Omega^*$, where reference data of the concentration is available, are generally disjoint. Then, the simulated concentration distribution is interpolated onto $\mathbf{x}^*$ to evaluate the deviation between simulation and reference. This way of projection is preferred as, in general, higher resolutions can be achieved in CFD simulations, and therefore, fewer interpolation errors are expected. For a reactive flow with the species $\psi \in \Psi = \{\psi_1, \psi_2, ..., \psi_{d_\Psi}\}$ with $d_\Psi \in \mathbb{N}$ representing the number of reactants, the reference concentration distribution of the reactant ψ is given as $c_\psi^* : \Omega^* \to \mathbb{R}, (\mathbf{x}^*) \mapsto c_\psi^*(\mathbf{x}^*)$. As its counterpart, we obtain the concentration distribution of the stationary solution from the CFD simulation, namely $c_\psi : \Omega_{\triangle x} \times \mathbb{R}^{d_\alpha} \to \mathbb{R}, (\mathbf{x}, \alpha) \mapsto c_\psi(\mathbf{x}, \alpha)$, also referred to as the *state*. The *controls* $\alpha \in \mathbb{R}^{d_\alpha}$ with $d_\alpha \in \mathbb{N}$ denoting the dimension of the control vector α, consist of the yet unknown reaction rate parameters, which are model parameters controlling the interaction of the reactants by the chemical reaction. Hereafter, $\mathbf{c} = (c_\psi)_\psi \in \mathbb{R}^{d_\Psi}$ and $\mathbf{c}^* = (c_\psi^*)_\psi \in \mathbb{R}^{d_\Psi}$ denote vectors of the reactants concentration distributions of the simulation and reference data set, respectively. The optimization problem minimizes for each re-

actant species ψ the deviation between c_ψ^* and the simulated stationary concentration field c_ψ by applying changes regarding the reaction rate parameters α. Thus, the goal of the optimization problem is to find the reaction parameters α where the resulting simulated concentration fields $\mathbf{c}$ have the minimal difference to the reference concentration distributions $\mathbf{c}^*$. Due to the assumption that our numerical model captures the same physics as in the reference data, the reaction rate parameters are inversely identified from the spatially distributed concentration fields $\mathbf{c}^*$. Thus, the inverse problem we aim to solve can be formulated as the following constrained optimization problem:

Find α and resulting concentration fields $\mathbf{c}$ such as:

$$\min_{\alpha} J(\mathbf{c}, \alpha) = \sum_{\psi \in \Psi} \left(\frac{\|c_\psi - c_\psi^*\|_{L^2(\Omega^*)}}{\|c_\psi^*\|_{L^2(\Omega^*)}} \right)^2, \tag{1}$$

while fulfilling constraints $\mathbf{G}(\mathbf{c}, \alpha) = \mathbf{0}$.

The *objective* $J : \mathbb{R}^{d_\Psi} \times \mathbb{R}^{d_\alpha} \to \mathbb{R}_0^+$ is minimized regarding the controls α where J is the sum of the squared relative errors between simulation and reference fields c_ψ and c_ψ^* for each reaction species ψ computed by the L^2-norm in Ω^*. In Sec. 3, the explicit formulation of (1) regarding the L^2-norm is given as this section aims to formulate the general optimization problem. While minimizing the objective function, constraints $\mathbf{G} = \mathbf{0}$ must be satisfied for each tuple of control variables α and resulting state $\mathbf{c}$. The choice of the constraint function is problem specific, whereas the following section specifies the applied constraint function in the presented work.

2.2. Constraint functions: coupled system of RADEs

Let us first assume that the reaction rate parameters α are known. Our work considers a homogeneous chemical reaction in a bulk flow, where the set of reacting species Ψ is transported by a carrier fluid via convection and diffusion. In general, such flow phenomena can be described by the RADE, given for the reactant ψ as

$$\partial_t c_\psi + \nabla_{\mathbf{x}} \cdot (c_\psi \mathbf{u}) = \nabla_{\mathbf{x}} \cdot (D_\psi \nabla_{\mathbf{x}} c_\psi) + R_\psi(\mathbf{c}) \quad \text{in } I \times \Omega, \tag{2}$$

where $I \in \mathbb{R}_0^+$ is the time space, $c_\psi : I \times \Omega \to \mathbb{R}, (t, \mathbf{x}) \mapsto c_\psi(t, \mathbf{x})$ the concentration distribution at time $t \in I$ and on the location $\mathbf{x} \in \Omega$, $\mathbf{u} \in \mathbb{R}^d$ the convective velocity, and $D_\psi > 0$ the scalar diffusivity constant. The chemical reaction couples the RADEs, modeling the local increase and decrease of the concentration in the distributions $\mathbf{c}$ by the source term $R_\psi : \mathbb{R}^{d_\Psi} \to \mathbb{R}$, given as

$$R_\psi(\mathbf{c}) = \sum_{r \in R} \nu_{r,\psi} \, \upsilon_r(\mathbf{c}), \tag{3}$$

where $r \in R$ corresponds to the rth reaction of in total of $R \subseteq \mathbb{N}$ reactions, the scalar $\nu_{r,\psi} > 0$ is the stochiometric constant, and $\upsilon_r : \mathbb{R}^{d_\Psi} \to \mathbb{R}$ the reaction rate. By applying the commonly used power law model for calculating the reaction rate, it reads

$$\upsilon_r(\mathbf{c}) = k_r \prod_{\psi \in P} c_\psi^{m_{r,\psi}}, \tag{4}$$

where $k_r > 0$ is the reaction constant of the reaction r, $P \subseteq \Psi$ are the reaction components participating on the rth reaction, and $m_{r,\psi} \geq 0 \in \mathbb{R}$ is the reaction order of the species ψ.

Returning to the parameter identification problem in (1), we first assume that the reactive flow problem from which the reference data $\mathbf{c}^*$ is obtained can be described by the equations (2), (3), and (4). Now, the reaction rate parameters are unknown, e.g., for a generic single chemical reaction of the equation $A + B \to C$ with $\Psi = \{A, B, C\}$, we want to identify the reaction constant and the reaction orders. That is, the control vector is given as $\alpha = (k, m_A, m_B)^{\mathrm{T}}$ with $d_\alpha = 3$ and the reaction rate law in (4) can be explicitly written as

$$v(\mathbf{c}, \boldsymbol{\alpha}) = k\, c_A^{m_A}\, c_B^{m_B}, \tag{5}$$

where the reaction rate $v : \mathbb{R}^{d_\psi} \times \mathbb{R}^{d_\alpha} \to \mathbb{R}$ now also depends on the controls. The optimization problem varies the parameters $\boldsymbol{\alpha} \in \mathbb{R}^{d_\alpha}$ to minimize the objective function (1). By omitting the time dependency due to the stationary assumption and by inserting (5) into (3) and then in (2), the simulated concentration field also depends on the controls as in (1), i.e., $c_\psi : \Omega \times \mathbb{R}^{d_\alpha} \to \mathbb{R}, (\mathbf{x}, \boldsymbol{\alpha}) \mapsto c_\psi(\mathbf{x}, \boldsymbol{\alpha})$. In our simulations, the coupled system of RADEs of (2) is solved numerically. Therefore, we consider only approximated solutions of the transport equations for the optimization problem, which is equal to fulfill the stationary RADEs as constraints $\mathbf{G} = \mathbf{0}$ with $\mathbf{G} = (G_\psi)_\psi \in \mathbb{R}^{d_\Psi}$. For the constraint function $G_\psi : \mathbb{R}^{d_\Psi} \times \mathbb{R}^{d_\alpha} \to \mathbb{R}$ for each reactant ψ, the RADEs are further simplified by assuming a uniform convective velocity field and isotropic diffusion, given as

$$G_\psi(\mathbf{c}, \boldsymbol{\alpha}) = \mathbf{u} \cdot \nabla c_\psi - D_\psi \Delta c_\psi - R_\psi(\mathbf{c}, \boldsymbol{\alpha}), \tag{6}$$

where $\mathbf{u} \in \mathbb{R}^d$ is the homogeneous convective velocity, $D_\psi > 0$ the scalar homogeneous diffusion constant of the species ψ, and $R_\psi : \mathbb{R}^{d_\Psi} \times \mathbb{R}^{d_\alpha} \to \mathbb{R}, (\mathbf{c}, \boldsymbol{\alpha}) \mapsto R_\psi(\mathbf{c}, \boldsymbol{\alpha})$ the reactive source term obtained by inserting (5) in (3).

3. Solution strategy for the parameter identification problem

This section outlines the applied discretization schemes in order to solve the formulated parameter identification problem in Sec. 2. To enable efficient identification of the reaction rate parameters, the quasi-Newton method L-BFGS [41,42], a fast converging gradient-based optimization method, and the LBM, an efficient discretization scheme to solve the coupled system of RADEs, are combined. First, in Sec. 3.1, the LBM scheme discretizing the constraint functions of Sec. 2.2 is described. Then in Sec. 3.2, the utilized optimization algorithm is presented, which classifies itself into the category of *first-discretize-then-optimize* approaches as described in [28].

3.1. LBM for solving the coupled system of RADEs

The system of constraint equations in (6) is solved numerically using the LBM with the multi-distribution function approach [43]. The discrete numerical domain $\Omega_{\triangle x} \subseteq \Omega$ is a homogeneous grid with the grid spacing $\triangle x \in \mathbb{R}$. On each grid node $\mathbf{x} \in \Omega_{\triangle x}$ the lattice Boltzmann equation for each species ψ is solved:

$$\begin{aligned} g_{i,\psi}(\mathbf{x} + \boldsymbol{\xi}_i \triangle t, t + \triangle t) \\ = g_{i,\psi}(\mathbf{x}, t) + \triangle t (q_{i,\psi}^C(\mathbf{x}, t) + q_{i,\psi}^S(\mathbf{x}, t, \boldsymbol{\alpha})) \quad \text{in } \Omega_{\triangle x} \times I_{\triangle t}, \end{aligned} \tag{7}$$

where $I_{\triangle t} \in I$ is the discrete time space with time steps $\triangle t \in \mathbb{R}$, $(\mathbf{x}, t)$ is defined in $\Omega_{\triangle x} \times I_{\triangle t}$, and $g_{i,\psi} : \Omega_{\triangle x} \times I_{\triangle t} \to \mathbb{R}$ is the discrete particle distribution function (PDF). For the particle velocities $\boldsymbol{\xi}_i \in \mathbb{R}^d$, the $D3Q7$ model from [14,44,45] is used, where the index $i \in \{0, 1, 2, ..., 6\}$ denotes the discrete velocity directions. The used stencil with the discrete velocity directions is shown in Fig. 2. The used discrete velocity vectors $\boldsymbol{\xi}_i$ are given in [45]. In (7), $q_{i,\psi}^C : \Omega_{\triangle x} \times I_{\triangle t} \to \mathbb{R}$ denotes the BGK collision operator [46], which models the linear relaxation of the PDFs towards their approximate thermodynamic equilibrium, given as

$$q_{i,\psi}^C(\mathbf{x}, t) = \frac{g_{i,\psi}^{eq}(\mathbf{x}, t) - g_{i,\psi}(\mathbf{x}, t)}{\tau_\psi}, \tag{8}$$

where $\tau_\psi > 0$ is the relaxation time. The linear equilibrium distribution $g_{i,\psi}^{eq} : \Omega_{\triangle x} \times I_{\triangle t} \to \mathbb{R}$ is written as

$$g_{i,\psi}^{eq}(\mathbf{x}, t) = w_i c_\psi(\mathbf{x}, t) \left(1 + \frac{(\boldsymbol{\xi}_i \cdot \mathbf{u})}{c_s^2} \right), \tag{9}$$

where $w_i \in \mathbb{R}_0^+$ are weighting terms as given in [45] and $c_s \in \mathbb{R}_0^+$ is a lattice constant, given as
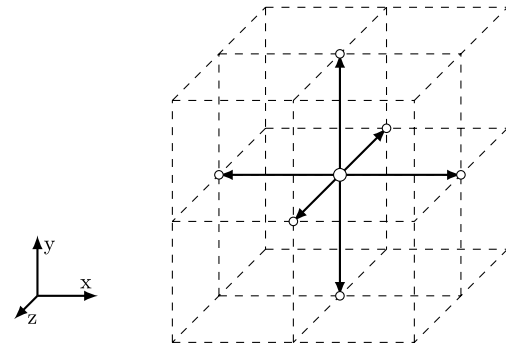

Fig. 2. Discrete velocity model $D3Q7$.

$$c_s = \frac{1}{2} \frac{\triangle x}{\triangle t} \tag{10}$$

for the $D3Q7$ model from [45], where $\triangle x$ and $\triangle t$ are chosen as unity in the dimensionless form. The chemical reaction is modeled by the source term $q_{i,\psi}^S : \Omega_{\triangle x} \times I_{\triangle t} \times \mathbb{R}^{d_\alpha} \to \mathbb{R}$ incorporated into (9) as in [47, 48], given by

$$q_{i,\psi}^S(\mathbf{x}, t, \boldsymbol{\alpha}) = w_i \left(1 - \frac{1}{2\tau_\psi} \right) R_\psi(\tilde{\mathbf{c}}, \boldsymbol{\alpha}), \tag{11}$$

where $\tilde{\mathbf{c}} = (\tilde{c}_\psi)_\psi \in \mathbb{R}^{d_\Psi}$ with $\tilde{c}_\psi : \Omega_{\triangle x} \times I_{\triangle t} \to \mathbb{R}$ being the zeroth order of the statistic moment, reading

$$\tilde{c}_\psi(\mathbf{x}, t) = \sum_{i=0}^{6} g_{i,\psi}(\mathbf{x}, t). \tag{12}$$

By updating the PDFs at every time step using (7), the macroscopic concentration field $c_\psi : \Omega_{\triangle x} \times I_{\triangle t} \times \mathbb{R}^{d_\alpha} \to \mathbb{R}$ for each species ψ is computed by

$$c_\psi(\mathbf{x}, t, \boldsymbol{\alpha}) = \tilde{c}_\psi + \frac{\triangle t}{2} R_\psi(\tilde{\mathbf{c}}, \boldsymbol{\alpha}), \tag{13}$$

where a correction of the statistic moment is required due to the source term [47,48]. After reaching the steady state, the time dependency of c_ψ in (13) can be omitted. In this work, diffusive scaling ($\triangle t \sim \triangle x^2 \to 0$) is applied to achieve convergence orders up to two as we do not solve an implicit equation in (13) as in [48]. The macroscopic diffusivity D_ψ of each component and the relaxation time are connected via

$$D_\psi = c_s^2 \left(\tau_\psi - \frac{\triangle t}{2} \right). \tag{14}$$

3.2. Gradient-based optimization algorithm

Now that we outlined how the coupled system of RADEs is solved, only the utilized optimization algorithm is missing. In order to solve the optimization problem in (1) numerically, an iterative gradient-based optimization algorithm is used. Algorithm 1 shows the steps performed by the implemented parameter identification framework. First, providing an initial guess regarding the reaction parameters $\boldsymbol{\alpha}^0$ is required. Then in step 1, the control parameters $\boldsymbol{\alpha}$ are set for the LBM simulation to compute the concentration distributions $\mathbf{c}^n$ by solving the coupled system of RADEs, where $n \in \mathbb{N}_0^+$ corresponds to the nth iteration step. That is, (7) is solved in each grid node in the numerical domain and for each time step until a steady state is reached. The concentration distributions $\mathbf{c}^n$ are obtained for the current $\boldsymbol{\alpha}^n$ by node-wise and species-wise evaluation of (13). In the next step, the concentration distributions are used to compute the objective function J^n in (1), i.e., the relative error between the simulation $\mathbf{c}^n$ and reference concentration fields $\mathbf{c}^*$ is calculated. For $N^* \in \mathbb{N}_0^+$ discrete positions $\mathbf{x}_i^* \in \Omega^*$ with $i \in N^*$ of available reference data points, the L^2-norm in (1) is computed as

Algorithm 1 Optimization algorithm to solve parameter identification problem.

Step 0: Choose initial guess of the controls $\boldsymbol{\alpha}^0$ (iteration step n = 0)

    Step 1: Compute concentration field $\mathbf{c}^n$ by running simulation with the parameters $\boldsymbol{\alpha}^n$

    Step 2: Compute objective J^n, i.e., relative error to the reference concentration fields $\mathbf{c}^*$

        If $J^n < \epsilon$ (alternatively $||\partial J^n/\partial\boldsymbol{\alpha}^n||_2 < \epsilon$, with $||\cdot||_2$ the Euclidean norm), then **stop**

        Else, **continue**

    Step 3: Compute derivatives $\partial J^n/\partial\boldsymbol{\alpha}^n$ to compute descent direction $\mathbf{d}^n$

        If step-size s^n is valid, update controls via $\boldsymbol{\alpha}^{n+1} = \boldsymbol{\alpha}^n + \triangle\boldsymbol{\alpha}^n$ and (17), then go to **Step 1**

        Else, adjust step-size s^n (this step involves function or derivative computation, i.e., a CFD simulation)

$$||\cdot||_{L^2(\Omega^*)} = \sqrt{\frac{1}{N^*}\sum_{i=1}^{N^*}(\cdot(\mathbf{x}_i^*))^2}. \tag{15}$$

Inserting (15) in (1), the objective function in the iteration step *n* explicitly yields

$$J^n(\mathbf{c}^n, \boldsymbol{\alpha}^n) = \sum_{\psi\in\Psi}\frac{\sum_{i=1}^{N^*}(c_\psi^n(\mathbf{x}_i^*, \boldsymbol{\alpha}^n) - c_\psi^*(\mathbf{x}_i^*))^2}{\sum_{i=1}^{N^*}(c_\psi^*(\mathbf{x}_i^*))^2}, \tag{16}$$

where the simulated concentration distribution c_ψ^n is interpolated onto the positions $\mathbf{x}^*$ to evaluate the deviation regarding the reference concentration. The algorithm terminates when the value of the objective function in (16) is lower than a user-specified threshold $\epsilon > 0$. If this is not the case, the sensitivities of the objective function regarding the controls $\partial J^n/\partial\boldsymbol{\alpha}^n \in \mathbb{R}^{d_\alpha}$ are computed either via forward finite difference quotients (FDQ) with a step size of half the machine precision (10^{-8}) or via the forward mode of algorithmic differentiation (AD) as applied in former studies [3,49]. The interested reader, regarding AD in general or the internal implementation of AD in OpenLB used in this work, is referred to the concise introduction by Griewank and Walther [50] or the work of Jeßberger et al. [49], respectively. As an alternative terminating condition, the Euclidean norm of the sensitivities is computed to check whether its magnitude is sufficiently low. The change in the controls $\triangle\boldsymbol{\alpha}^n \in \mathbb{R}$ is given as

$$\triangle\boldsymbol{\alpha}^n = s^n\mathbf{d}^n, \tag{17}$$

where $s^n \in \mathbb{R}_0^+$ is the step size and $\mathbf{d}^n \in \mathbb{R}^{d_\alpha}$ the descent direction of the current iteration step *n*. Armijo and Wolfe rules are applied to find appropriate step sizes s^n balancing stability and convergence speed [41,42]. Therein, the appropriate step size is found by applying iterative changes, i.e., an additional inner loop performs several function or gradient evaluations containing CFD simulations. When both rules are satisfied for a computed step size $\triangle\boldsymbol{\alpha}^n$, the performed simulation with $\boldsymbol{\alpha}^{n+1} = \boldsymbol{\alpha}^n + \triangle\boldsymbol{\alpha}^n$ is counted as a valid optimization step. L-BFGS [29] computes the descent direction $\mathbf{d}^n$ using the objective derivatives obtained by either FDQ or AD. After updating the control variables, the algorithm returns to step 1, repeating the steps until satisfying the termination condition.

4. Validation

To investigate the feasibility of the presented method and to validate the results, a benchmark test case is constructed. The concentration distributions obtained by a CFD simulation with *a priori* known reaction rate parameters are used to compute the reference concentration fields $\mathbf{c}^*$. Then, these reference fields are fed into the parameter identification framework recovering the reference reaction rate parameters. Fig. 3 schematically illustrates the parameter identification framework and the validation process where some measurement data is replaced by a

reference CFD simulation. Having the goal in mind to apply this method to real measurement data, various scenarios for the reference data are investigated, such as modifying the reference concentration distribution by statistical noise. All presented methods introduced in this study are implemented with the open-source software library OpenLB [39,40].

As a side note, we also conduct studies using the method of steepest descent instead of L-BFGS. However, the results only varied in terms of convergence speed, i.e., the L-BFGS required less optimization steps compared to steepest descent. Thus, the following work only presents the results produced by L-BFGS.

4.1. Benchmark case: bulk reaction between two parallel plates

A quasi-2D bulk flow between two opposing plates is considered where reaction species *A* and *B* diffuse from the bottom and top plate surfaces, respectively, as shown in Fig. 4. The two species are transported from left to right via a homogeneous velocity field. The vertical distance between the plates is given by the height $H = 0.16\,\mathrm{m}$ and the plate length as $L = 1.6\,\mathrm{m}$, yielding a geometrical ratio of $H/L = 0.1$. The benchmark case models the homogeneous chemical reaction $A + B \to C$ in the bulk. The homogeneous velocity field $\mathbf{u}$ transports the reaction species in the flow direction, and the source term R_ψ of (4) creates species *C* via chemical reaction depending on the local concentrations c_A and c_B. The diffusivity of all species in the carrier fluid is set equal, thus all diffusion constants collapse to a single variable *D*. The Péclet number of the current flow problem is defined as

$$Pe = \frac{u_x H}{D}, \tag{18}$$

for all reaction species, where u_x is the flow velocity in *x*-direction.

The reference simulation is performed with the LBM scheme presented in Sec. 3. The grid resolution for the reference solution is chosen as $H \times L \times Z = 40 \times 400 \times 1$ cells, leading to a grid step size of $\triangle x = 0.004\,\mathrm{m}$ with a temporal step size of $\triangle t = 1.6 \times 10^{-5}\,\mathrm{s}$. The simulation domain consists of $N_\psi = 16 \times 10^3$ grid points for each species ψ. The spatial position in flow direction *x* is defined as $0 \geq x \geq L$ and its normal direction *y* as $0 \geq y \geq H$. Periodic boundary conditions are applied in the depth direction *z* in $0 \geq z \geq Z$ with a grid resolution of one grid cell for the depth $Z \in \mathbb{R}$. At the remaining four boundaries $\Gamma_\mathrm{in}, \Gamma_\mathrm{out}, \Gamma_\mathrm{top}, \Gamma_\mathrm{bottom} \subseteq \Omega$, Dirichlet and Neumann-type boundary conditions are applied as depicted in 4. At the inflow Γ_in with $(x = 0, y, z)$, the inflow concentration $c_{\psi,\mathrm{in}}$ is set to zero for all species ψ. At the outflow Γ_out with $(x = L, y, z)$, the free-stream condition is applied, i.e., $\partial c_{\psi,\mathrm{out}}/\partial x = 0$. The following boundary conditions are applied at the top plate Γ_top with $(x, y = H, z)$ and bottom plate Γ_bottom with $(x, y = 0, z)$ for each reaction species ψ:

$$\Gamma_\mathrm{top}: \quad \psi = \begin{cases} A, & \frac{\partial c_A}{\partial y} = 0, \\ B, & c_B = c_\mathrm{wall}, \\ C, & \frac{\partial c_C}{\partial y} = 0, \end{cases}$$

and

$$\Gamma_\mathrm{bottom}: \quad \psi = \begin{cases} A, & c_A = c_\mathrm{wall}, \\ B, & \frac{\partial c_B}{\partial y} = 0, \\ C, & \frac{\partial c_C}{\partial y} = 0. \end{cases} \tag{19}$$

In the current LBM model, all Dirichlet-type boundary conditions are applied via the moment-based boundary condition as in [51] and for the Neumann-type zero gradient boundary condition, the identical schemes as in [14,49] are used. The convective flow velocity is prescribed as $\mathbf{u} = (0.05 \times 10^{-3}, 0.0, 0.0)^\mathrm{T}$ m/s and the Péclet number as $Pe = 108$ leading to a diffusivity of $D = 7.407 \times 10^{-8}\,\mathrm{m}^2/\mathrm{s}$. For reaction rate parameters, the reaction constant is set to $k^* = 1.2 \times 10^{-6}(\mathrm{kg/m}^3)^{1-(m_A^*+m_B^*)}/\mathrm{s}$, the reaction order of species A to $m_A^* = 1.3$, the reaction order of species B to $m_B^* = 1.1$. Hereafter, these parameters are referred to as *reference parameters* $\boldsymbol{\alpha}^* \in \mathbb{R}^3$, given as
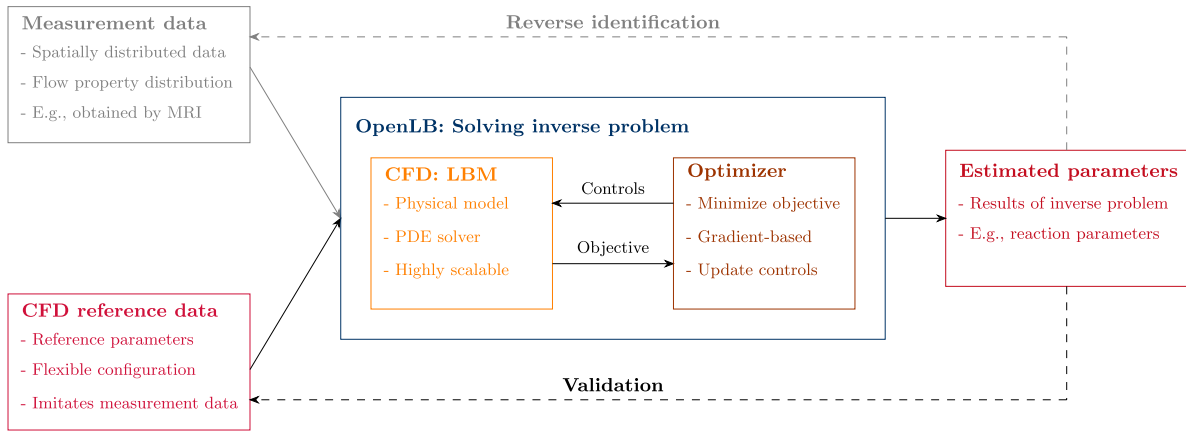
Fig. 3. Parameter identification framework in OpenLB. The concentration field of a CFD simulation with prior known reaction rate parameters is used for the reference concentration field to validate the identification process.
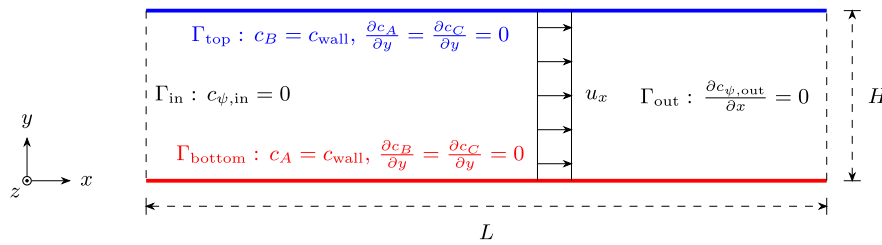

Fig. 4. Reactive flow problem considered in the benchmark case: Two opposing plates with fixed surface concentration where the species are transported via homogeneous convection field and diffusion. The applied boundary conditions are depicted in the schematic view of the flow problem.
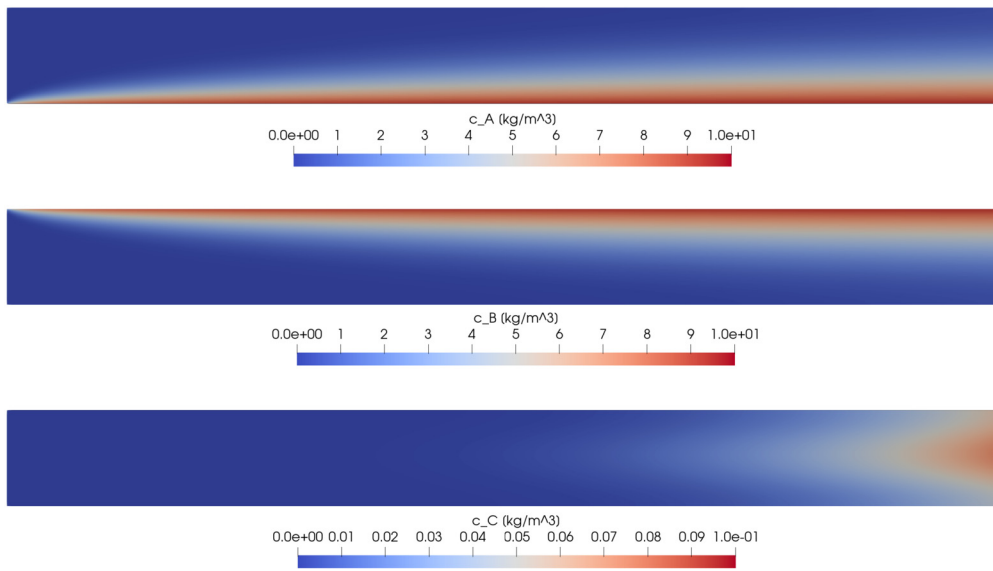

Fig. 5. Reference concentration distributions c_ψ^* for all species A, B, and C (from top to down) obtained for the reference parameter set $\boldsymbol{\alpha}^*$ of (20).

$$\boldsymbol{\alpha}^* = (k^*, m_A^*, m_B^*)^{\mathrm{T}} = (1.2 \times 10^{-6}, 1.3, 1.1)^{\mathrm{T}}. \tag{20}$$

Simulating with $\boldsymbol{\alpha}^*$ until reaching a steady state gives the reference concentration field $\mathbf{c}^*$ for each reaction species ψ, presented in Fig. 5.

A grid independence study is conducted to ensure grid convergence of the simulated flow problem. The grid spacing $\triangle x$ is varied such that the total number of grid cells ψ doubles in each increasing refinement level. Fig. 6 shows the investigated experimental order of convergence (EOC) regarding the product concentration $\bar{c}_C$ averaged over the whole domain Ω. In the current simulation, three reaction species are trans-

ported via three RADEs, which are all solved on the same numerical grid but involving three times solving (7). That is, the total number of cells updated each time step is given as $N = \sum_{i \in d^\Psi} N_\psi$, which is the sum of the grid cells over the number of solved RADEs. Since no analytic solution is available for this flow problem, the difference of the averaged product concentration between the simulation with the resolution with $N^{\text{finest}} = 6129120$ and a simulation with the grid resolution N with $N < N^{\text{finest}}$ total number of cells is computed as

$$Err_{\bar{c}_{C,\Omega}^N} = (\bar{c}_{C,\Omega}^N - \bar{c}_{C,\Omega}^{N^{\text{finest}}})^2, \tag{21}$$
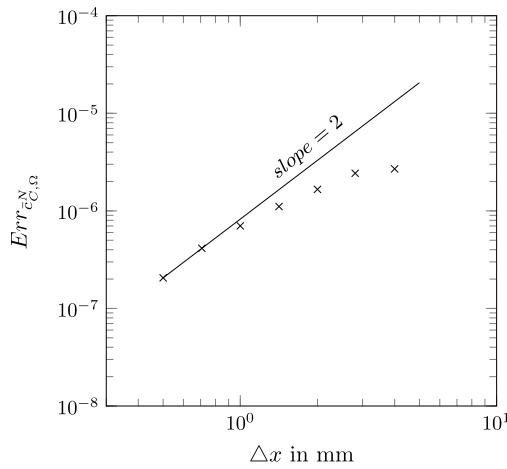
Fig. 6. EOC is studied for the presented reactive flow simulation as shown in Fig. 5. The difference of the average product concentration $\bar{c}_{C,\Omega}^N$ over Ω to its value of the simulation at the highest resolution $\bar{c}_{C,\Omega}^{N^{\text{finest}}}$ with $N^{\text{finest}} = 6129120$ is computed via (21) and plotted over the grid spacing $\triangle x$ in millimeters.

where $\bar{c}_{C,\Omega}$ denotes the averaged product concentration over Ω, the upper index N the current resolution, and N^{finest} the highest resolution. The decrease of the computed error in (21) approaches the second order with increasing grid resolution as demonstrated in Fig. 6. That is, for the species A at the left lower corner ($x = 0, y = 0, z$) and the species B at the upper left corner ($x = 0, y = H, z$), the zero inflow concentration collides with the non-zero concentration prescribed at the wall by Dirichlet-type boundary conditions causing errors independent of the grid resolution. However, by increasing the overall resolution of the simulation, the influences of that disturbance diminish compared to the overall flow, explaining why the error approaches a second-order function with respect to $\triangle x$ for high resolution.

4.2. Identification of reaction rate parameters

The reaction rate parameters are identified for the bulk reaction benchmark case. If not explicitly stated differently, the algorithm terminates when the gradient magnitude of the objective function decreases below the threshold of $\epsilon = 10^{-8}$. Here, the objective gradient is preferred over the actual value of the objective function for the terminating condition since, in most cases, the objective value at the local minima is not known *a priori*. AD is implemented via operator overloading in C++ and is already tested in previous studies such as in [3,49]. The simulation performed in the parameter identification process is conducted on the identical numerical grid as of the reference simulation, i.e., $\Omega_{\triangle x} = \Omega^*$, with a total number of $N = \sum_{\psi \in \Psi} N_\psi = 48 \times 10^3$ cells updated for all three species. The bulk reaction benchmark case is investigated for five different configurations (case A to case E, see Fig. 7) of the reference concentration distribution. In the first configuration (case A), the objective function in (16) is computed only using the concentration field of species A. Hereafter, if not explicitly stated differently, only the concentration field c_A^* is used as the reference field to recover the parameters in all conducted cases. Then, case A is investigated regarding the dimension of the control vector d_α, grid dependency, influences of the chosen algorithm to compute the gradients, and different reference parameters α^*. In case B, only the concentration in the cells one layer in front of the outflow is considered for the reference data set. By this, the reference data contains only the 1D concentration distribution at the outflow. Furthermore, different initial guesses α^0 are chosen to investigate the robustness of the identification process for this case with reduced data sets. To demonstrate the importance of using spatially distributed data for solving the inverse problem, case C tries to identify the reference parameters by only comparing the outlet product concentration between simulation and reference simulation. Case D aims to

imitate MRI measurement data by inducing noise signals onto the reference concentration field, adding uncertainty to the data. Finally, case E investigates the influences of having lower grid resolutions for the reference simulation introducing new sources of errors, i.e., discretization and interpolation errors.

4.2.1. Case A: whole concentration distribution of one species

In case A, the whole concentration field of species A is used as the reference field, whereby the objective sensitivities are computed by AD. First, the influence of the number of simultaneously identified parameters, i.e., the dimension d_α of the control vector α, on the parameter identification process is investigated. The Figs. 8a-8c presents the results for the one-dimensional case ($d_\alpha = 1$) where the control vector consists of the reaction constant $\alpha = (k)^{\text{T}}$. The initial guess of the reaction constant $\alpha^0 = 0.1 \times 10^{-6} (\text{kg}/\text{m}^3)^{1-(m_A+m_B)}/\text{s}$ contains an initial relative error of 91% to its reference value. Fig. 8a shows the development of the control variable α^n over the performed number of simulations. The solid line with the corresponding color indicates the reference parameter, which is recovered by the presented method. Fig. 8b plots the relative error regarding the parameters $\Delta\alpha_{i,\text{rel}}^n$ and Fig. 8c the absolute value of the relative error of the averaged outflow product concentration $\Delta\bar{c}_{\text{rel}}^n$, given as

$$\Delta\alpha_{i,\text{rel}}^n = \frac{\alpha_i^* - \alpha_i^n}{\alpha_i^*} \quad \text{and} \quad \Delta\bar{c}_{\text{rel}}^n = \frac{\bar{c}_{C,\text{out}}^* - \bar{c}_{C,\text{out}}^n}{\bar{c}_{C,\text{out}}^*}, \tag{22}$$

respectively. The plots depict the convergence of the control parameter towards its reference value in 20 simulations corresponding to 5 optimization steps. Our method reduces the initial relative error from 91% to 10^{-6}% regarding the control parameter as well as for the averaged outflow concentration. As we increase the number of control parameters from one to two, the algorithm still converges towards their corresponding reference values, as we see in Fig. 8d-8f. Here the reaction constant and the reaction order of the species A are recovered simultaneously, starting with the initial guess given as $\alpha^0 = (k^0, m_A^0)^{\text{T}} = (0.1 \times 10^{-6}, 0.8)^{\text{T}}$. The accuracy by additionally recovering the reaction order of species A drops slightly to a final relative error of 10^{-5}%. The number of required simulations increases to 26 with 8 optimization steps. Similar results are obtained by further increasing the dimension of the control vector by including the reaction order of species B demonstrated in Fig. 8g-8i. Even for three parameters with the initial guess of $\alpha^0 = (k^0, m_A^0, m_B^0)^{\text{T}} = (0.1 \times 10^{-6}, 0.8, 0.8)^{\text{T}}$, the control parameters converge towards their corresponding reference parameters. For all plots in Fig. 8, the number of required simulations increases, while the accuracy of the found parameters and the resulting product concentration decrease as the dimension of the control vector increases. However, for $d_\alpha = 3$, the accuracy of the found parameters is still in a high range of 10^{-3}% while necessitating only 37 simulations corresponding to 13 optimization steps as demonstrated in Fig. 8h. Furthermore, case A with $d_\alpha = 3$ is investigated for different reference parameters, given as:

$$\alpha_I^* = \begin{pmatrix} 1.2 \times 10^{-6} \\ 1.3 \\ 1.1 \end{pmatrix}, \quad \alpha_{II}^* = \begin{pmatrix} 2.2 \times 10^{-6} \\ 2.3 \\ 2.1 \end{pmatrix}, \quad \alpha_{III}^* = \begin{pmatrix} 3.2 \times 10^{-6} \\ 3.3 \\ 3.1 \end{pmatrix}. \tag{23}$$

The results in Fig. 9 demonstrate the successful recovery of the reaction rate parameters by using the reference parameters given in (23). The optimization algorithm effectively minimizes the magnitude of the vector containing the relative errors $\Delta\alpha_{\text{rel}}^n$ computed by the Euclidean norm $|| \cdot ||_2$ as well as the relative error in average product concentration at the outflow $\Delta\bar{c}_{\text{rel}}^n$.

Next, the influence of the grid resolution on the parameter identification process is investigated. Fig. 10a presents the development of the relative error regarding the found reaction parameters for the total number of grid cells of $N = 48 \times 10^3$, 96×10^3, and 192×10^3 cells for dif-
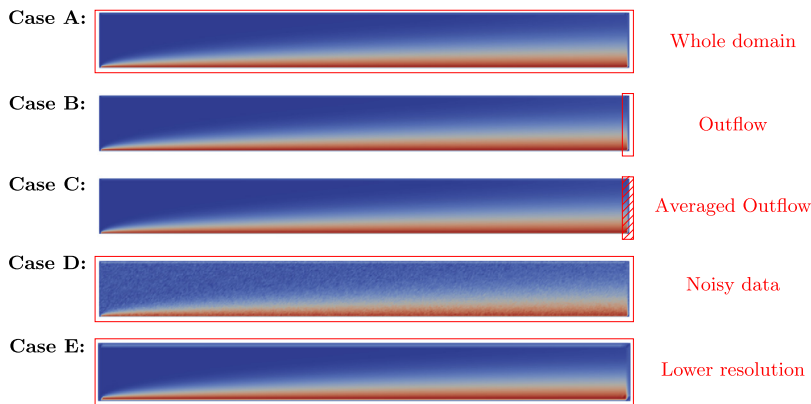
Fig. 7. Overview of investigated cases (A to E) with various configurations of the reference concentration field, here illustrated for c_A^*.

(a) $d_\alpha = 1$, controls

(b) $d_\alpha = 1$, relative error controls

(c) $d_\alpha = 1$, relative error product

(d) $d_\alpha = 2$, controls

(e) $d_\alpha = 2$, relative error controls

(f) $d_\alpha = 2$, relative error product

(g) $d_\alpha = 3$, controls

(h) $d_\alpha = 3$, relative error controls

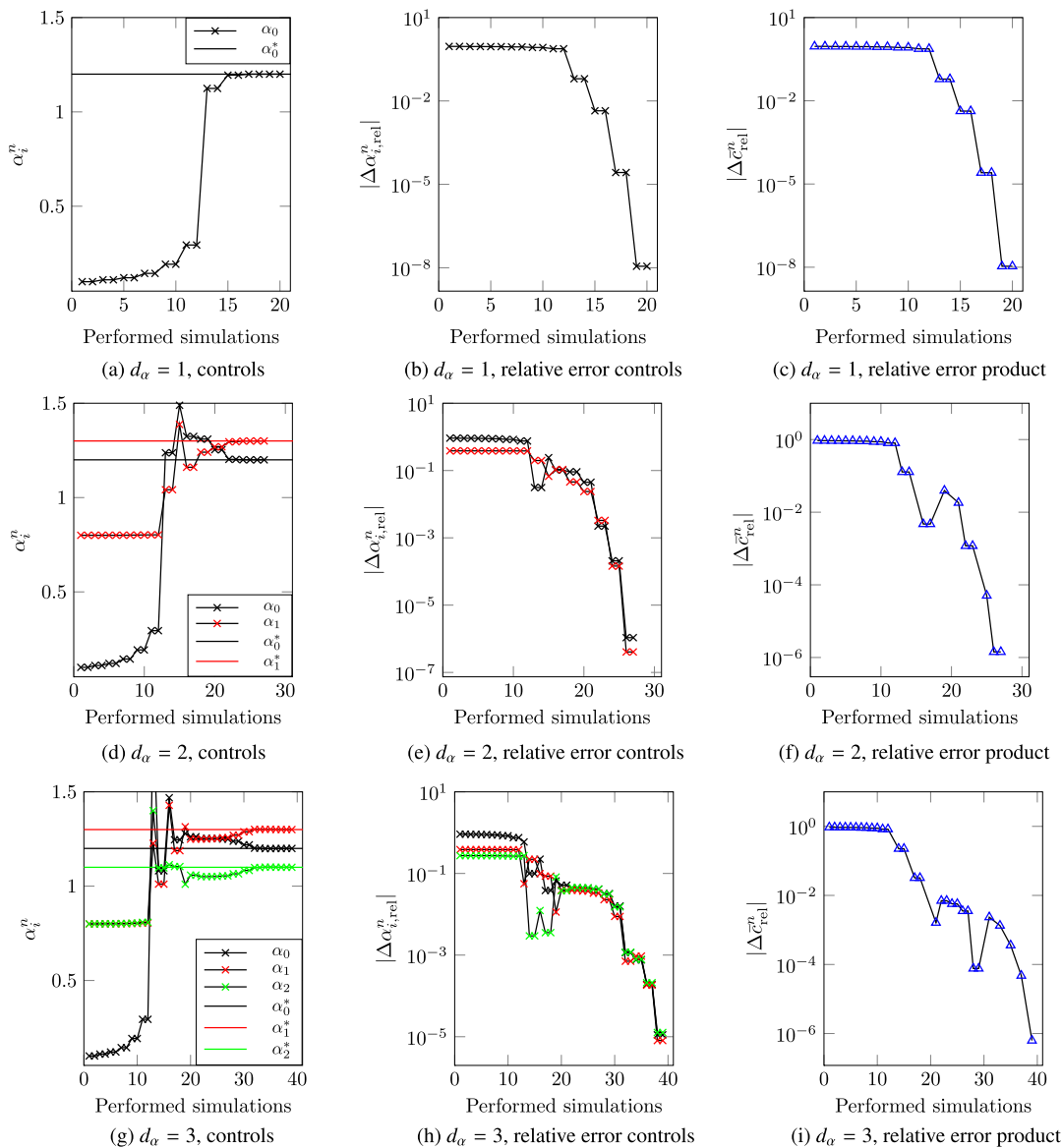(i) $d_\alpha = 3$, relative error product

Fig. 8. Case A: Recovery of the reaction rate parameters from including only the reference concentration c_A^*. The dimension d_α of the control vector is increased from one up to three parameters recovered in a single optimization problem (row-wise, from top to bottom). The values of the control vector, the relative error of the controls to its reference values, and the relative error of the averaged product outflow concentration are plotted over the performed number of simulations (column-wise from left to right). The ticks depict the actual values of the controls at a performed simulation. Note the change in the x-axis over the rows and the scaling of the reaction constant to the same order as the reaction orders for better visualization.
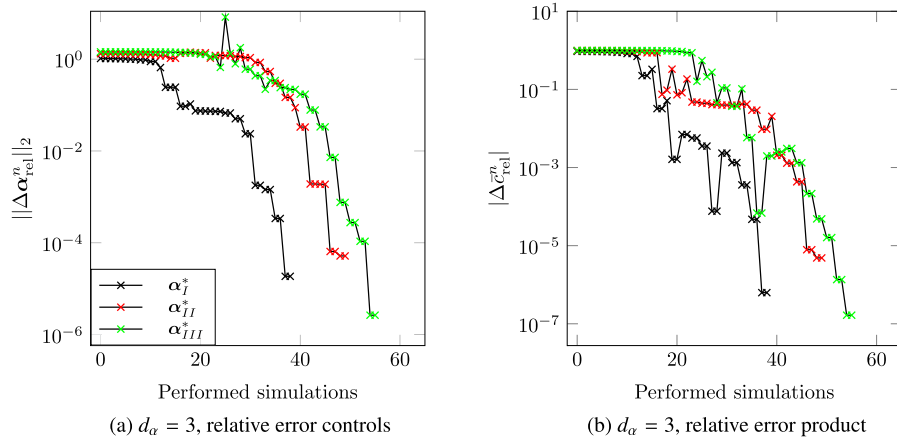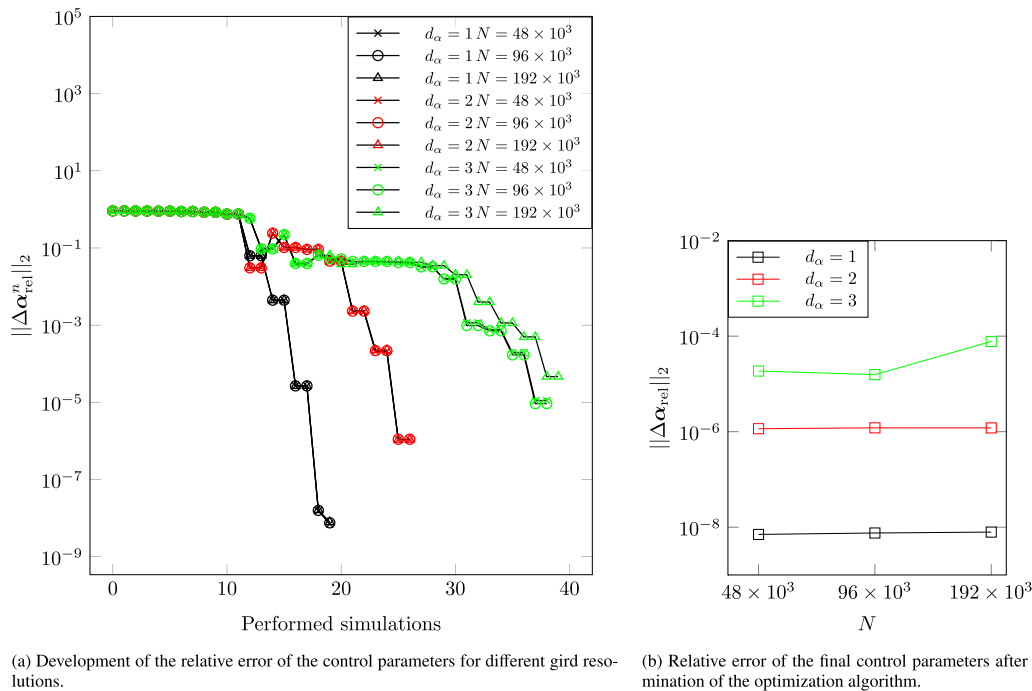
(a) $d_\alpha = 3$, relative error controls

(b) $d_\alpha = 3$, relative error product

Fig. 9. Case A: The reference parameters $\boldsymbol{\alpha}^*$ are varied to test the optimization problem with various rate law formulations regarding the control variables. For all tested reference parameters in (23), the presented method successfully identifies the reference reaction rate parameters.

(a) Development of the relative error of the control parameters for different grid resolutions.

(b) Relative error of the final control parameters after termination of the optimization algorithm.

Fig. 10. Case A: Influence of the grid resolution on the parameter identification. AD is used here for the gradient computation.

ferent control dimensions. Note that here the resolution of the reference simulation and the simulations during the optimization is scaled accordingly, whereby the case where they vary is studied in case E (Sec. 4.2.5). For $d_\alpha = 1$ and $d_\alpha = 2$, there are no visible differences in the optimization steps as well as in the final relative error in the found reaction parameters. For $d_\alpha = 3$, there is a slight difference at the highest grid resolution, which is likely due to a round-off error leading to the outlier behavior. However, the results in Fig. 10a indicate grid independence regarding the investigated optimization problem.

Finally, the influence of the different algorithms to compute the objective gradient is investigated together with the scaling performance of the presented algorithm. The implemented framework is executed on eight message-passing interface (MPI) processes on an AMD Ryzen Threadripper 2990WX 32-Core Processor. Fig. 11a illustrates the total necessitated running time t_{total} in minutes to solve the inverse problem regarding the dimension of the control vector and grid resolution. Fig. 11b presents the development of the relative error regarding the control variables for AD and FDQ. It is notable that for three control parameters using the FDQ requires almost twice as many simulations

compared to AD but half the total running time to solve the inverse problem. The reason for this is that AD changes the LB data structure from a performance-optimized *structure-of-arrays* (SoA) [27] to a *structure-of-arrays-of-structures* (SoAoS) while FDQ leaves the core data structure unchanged. The SoAoS emerges for AD due to the usage of a custom, control-parameter-dependent structure as the foundational arithmetic type of the entire simulation. Fig. 12a compares the scaling behavior in terms of throughput in mega lattice updates per second (MLUPs) between using FDQ (blue) and AD (red). Different scaling behavior regarding the dimension of the control variable and the grid resolution is observed. For the grid resolution of $N = 96 \times 10^3$ cells, the MLUPs are nearly constant for FDQ, while using AD, there is a visible dependency of the number of computed derivatives and the performance as shown in Fig. 12b. It has to be noted that the maximum resolution of 192×10^3 cells is comparably small and below the scope of scaling optimizations in OpenLB, which commonly target higher resolutions up to billions of cells. While small problem sizes provide a possible advantage due to better cache utilization, this is best utilized in combination with vectorized (SIMD) execution which is currently not
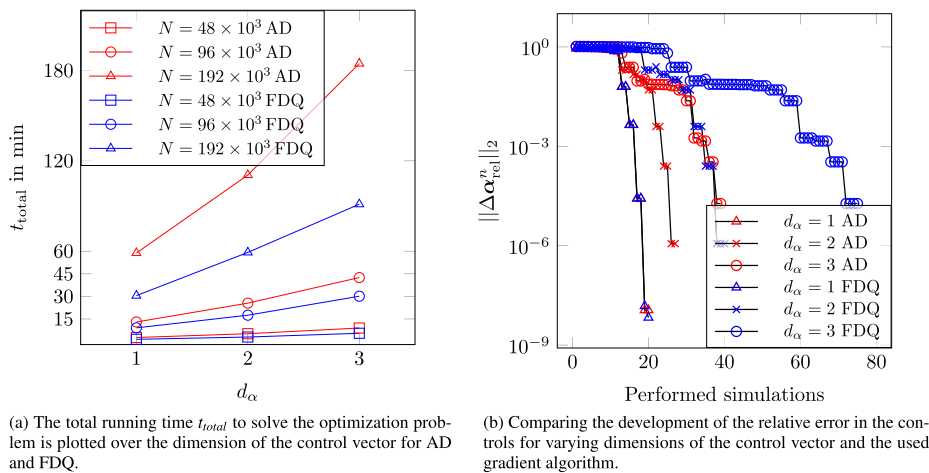
(a) The total running time t_{total} to solve the optimization problem is plotted over the dimension of the control vector for AD and FDQ.

(b) Comparing the development of the relative error in the controls for varying dimensions of the control vector and the used gradient algorithm.

Fig. 11. Case A: Comparison of the two applied algorithms to compute the objective sensitivities, i.e., AD and FDQ, regarding the optimization problem and required total running time.
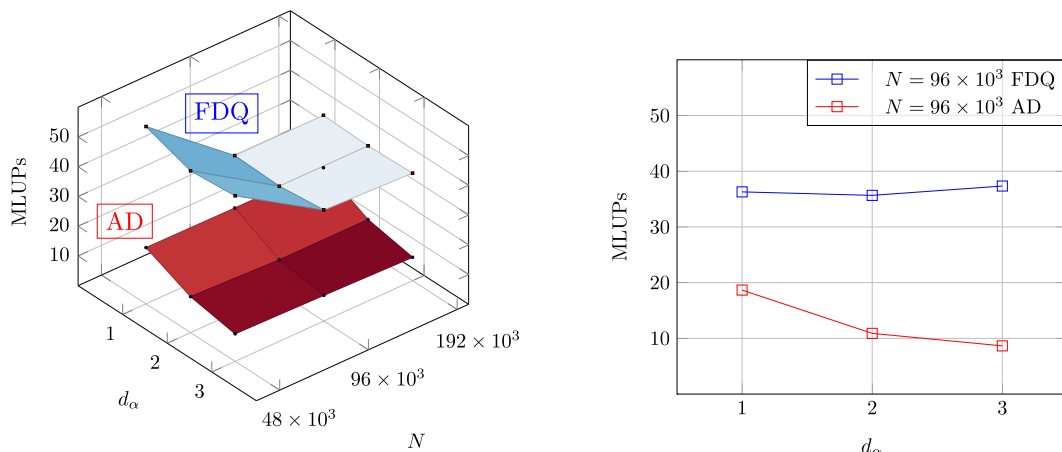

(a) Performance dependency on the number of control variables d_α, grid resolution, and chosen gradient algorithm. The upper plane (blue) corresponds to the measured MLUPs obtained in the simulation with floating-point types used for computing gradients with FDQ, and the plane below (red) to the simulation where AD types are used.

(b) A segment of the graph on the left for $N = 96 \times 10^3$. The dependency of the AD-type on the number of calculated derivatives, i.e., the sensitivity regarding each control parameter, is illustrated.

Fig. 12. Case A: Scaling behavior compared for the both implemented gradient algorithms, FDQ and AD.

Table 1

The highest achieved accuracy regarding the recovered reaction rate constant using AD and FDQ by setting the termination condition ϵ in Algorithm 1 to machine precision, i.e., $\epsilon = 10^{-16}$.

Gradient computation	Relative error control
AD	4.422×10^{-14}
FDQ	4.167×10^{-9}

supported for AD and was not enabled for FDQ to ensure a fair comparison. Future performance-focused work should split the foundational AD type into a plain SoA structure to enable vectorization in addition to using automatic code generation specifically targeted at the critical AD collision kernels. Although there are currently significant performance drawbacks in using AD, its main advantage lies in the accuracy of the computed gradients compared to FDQ. Since AD does not suffer from cancellation due to round-off errors, as in the case of FDQ, AD allows more accurate computations of the objective gradients. Table 1 compares the highest achieved accuracy of the recovered reaction rate parameters for case A with $d_\alpha = 1$ by setting the terminating condition ϵ equal to machine precision.

While the FDQ could only reach relative errors of roughly the step size chosen for the difference stencil, AD gets almost machine-precision accurate results. For $\epsilon = 10^{-8}$, no significant influence on the result of the optimization problem is observable, as shown in Fig. 11b. However, in the following, AD is preferred over FDQ to compute the objective gradients as performance is not the main focus in those cases.

4.2.2. Case B: outflow concentration distribution of one species

This case reduces the number of accessible grid points of the reference simulation to only those positioned one layer next to the outflow region for the inverse problem. This corresponds to a reduction of 99.75% regarding the accessible information about the reference concentration field compared to the previous case. The presented method still recovers the control parameters for the identical initial guesses as given in (20), see Fig. 13. The final relative error, in this case, is in the same order as in case A, as shown in Fig. 13a. Regarding the number of required simulations, there are slightly more simulations involved for $d_\alpha = 3$. Several initial guesses are tested to investigate the robustness of the optimization problem. Table 2 lists six different initial guesses picked from an interval, where the reference parameters could be recovered successfully. Fig. 14 confirms the convergence of the parameters towards the reference parameters as the relative error
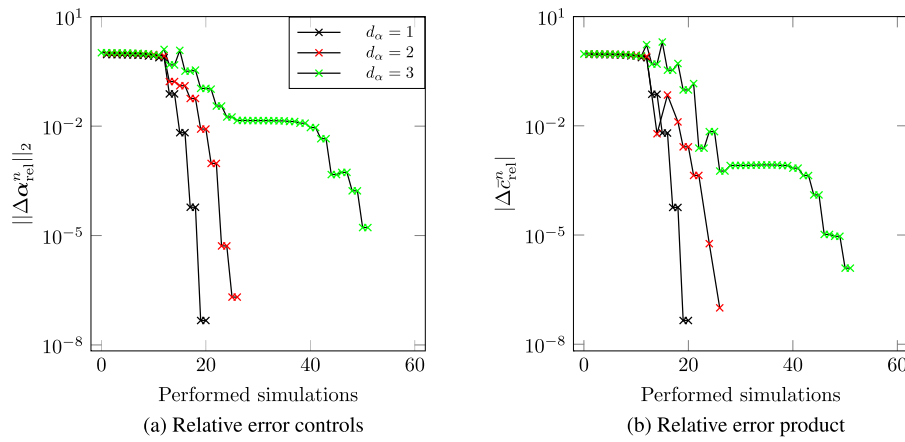
(a) Relative error controls

(b) Relative error product

Fig. 13. Case B: In this case, only the reference concentration distribution at the outflow is used to recover the reaction rate parameters. Even after this reduction, all three reaction rate parameters could be identified from the reference data.
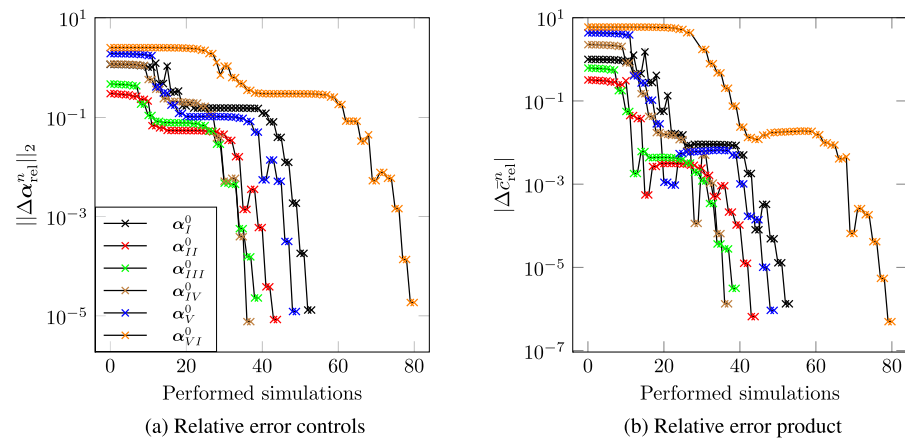

(a) Relative error controls

(b) Relative error product

Fig. 14. Case B: Development of the relative error regarding the controls for the picked initial values in Table 2 where again only the reference concentration distribution at the outflow is used to recover the reference parameters.

Table 2

List of six different initial guesses $\boldsymbol{\alpha}^0$ (I to VI) picked from an interval, where the presented method successfully recovered the reference parameters. The values for the reaction constant k^0, reaction order m_A^0 of species A, and reaction order m_B^0 of species B are listed below. The corresponding value $||\Delta\boldsymbol{\alpha}_{\text{rel}}^0||_2$ is computed as a measure for the distance of the initial guess from the reference parameters $\boldsymbol{\alpha}^*$ by (22).

$\boldsymbol{\alpha}^0$	k^0	m_A^0	m_B^0	$||\Delta\boldsymbol{\alpha}_{\text{rel}}^0||_2$
$\boldsymbol{\alpha}_I^0$	1.0×10^{-11}	0.7	0.7	1.16
$\boldsymbol{\alpha}_{II}^0$	1.0×10^{-6}	1.0	1.0	0.30
$\boldsymbol{\alpha}_{III}^0$	1.5×10^{-6}	1.5	1.5	0.47
$\boldsymbol{\alpha}_{IV}^0$	2.0×10^{-6}	2.0	2.0	1.18
$\boldsymbol{\alpha}_V^0$	2.5×10^{-6}	2.5	2.5	1.91
$\boldsymbol{\alpha}_{VI}^0$	3.0×10^{-6}	3.0	2.8	2.52

regarding the controls is successfully reduced. Choosing combinations of lower values regarding reaction constant/orders than in $\boldsymbol{\alpha}_I^0$ or higher values than in $\boldsymbol{\alpha}_{VI}^0$ leads to divergence of the simulation, and therefore, the optimization problem is not able to recover the reference parameters. The results of the current case demonstrate that even reducing the spatial dimension of the reference data from 2D to 1D data still suffice to recover reaction rate parameters reliably in the presented benchmark problem.

4.2.3. Case C: averaged outflow concentration

In this case, we purposely omit the use of spatially distributed data for the inverse problem to investigate whenever ambiguity problems are occurring. Following the previous case, the reference data is further reduced to the averaged concentration at the outflow. This requires a different formulation of the objective function, giving for species A:

$$J_{\text{case C}}(\mathbf{c}^n, \boldsymbol{\alpha}^n) = \left(\bar{c}_{A,\text{out}}^* - \bar{c}_{A,\text{out}}^n(\boldsymbol{\alpha}^n)\right)^2, \tag{24}$$

where $\bar{c}_{A,\text{out}}$ indicates the average concentration of species A on a single grid layer at the outflow. Fig. 15a shows the relative error of the control parameters for using (24) as the objective function using only the averaged concentration of species A. For more than one control parameter ($d_\alpha > 1$), the optimization problem is unable to find a unique solution regarding the reaction rate parameters. By adjusting the objective function depending on the number of control parameters as

$$J_{\text{case C}}(\mathbf{c}^n, \boldsymbol{\alpha}^n, d_\alpha)$$

$$= \begin{cases} d_\alpha = 1, & \left(\bar{c}_{A,\text{out}}^* - \bar{c}_{A,\text{out}}^n\right)^2, \\ d_\alpha = 2, & \left(\bar{c}_{A,\text{out}}^* - \bar{c}_{A,\text{out}}^n\right)^2 + \left(\bar{c}_{B,\text{out}}^* - \bar{c}_{B,\text{out}}^n\right)^2, \\ d_\alpha = 3, & \left(\bar{c}_{A,\text{out}}^* - \bar{c}_{A,\text{out}}^n\right)^2 + \left(\bar{c}_{B,\text{out}}^* - \bar{c}_{B,\text{out}}^n\right)^2 + \left(\bar{c}_{C,\text{out}}^* - \bar{c}_{C,\text{out}}^n\right)^2, \end{cases}$$

$$\tag{25}$$

the control parameters converge towards the reference parameters as demonstrated in Fig. 15b. The number of performed simulations in-
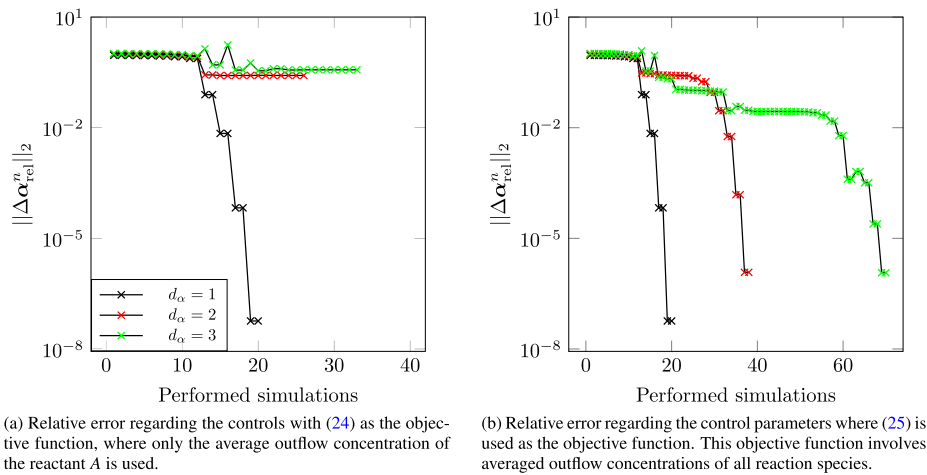
(a) Relative error regarding the controls with (24) as the objective function, where only the average outflow concentration of the reactant A is used.

(b) Relative error regarding the control parameters where (25) is used as the objective function. This objective function involves averaged outflow concentrations of all reaction species.

Fig. 15. Case C: Using Averaged Outflow concentrations for the parameter identification problem. Here the optimization problem faces ambiguity problems when the objective function in (24) is used.

(a) Relative error controls

(b) Objective function
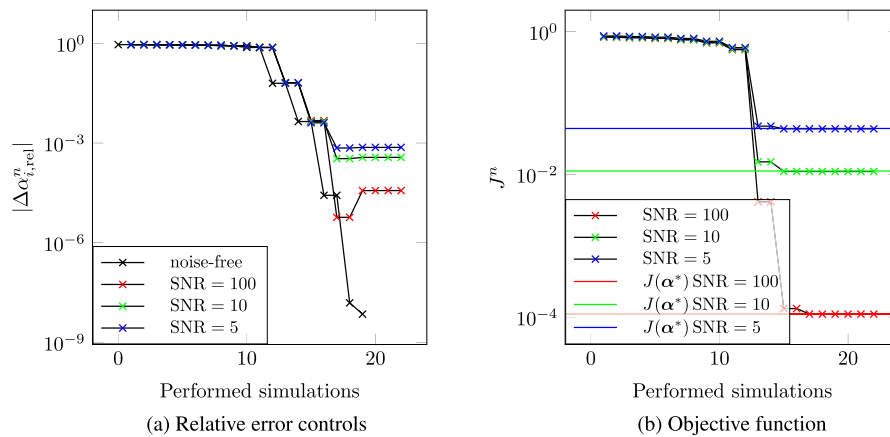
Fig. 16. Case D: Inducing statistical noise onto the reference solution, compared for different noise intensities ($d_\alpha = 1$).

creases compared to the previous two cases by increasing the number of simultaneously recovered parameters. However, adapting the objective function for more complex inverse problems involving more reaction rate parameters is not trivial and could require sophisticated approaches such as regularization to solve ambiguity problems. This case showcases once again, how recovering kinetic parameters from punctual/integral measurements is an difficult and error-prone task.

4.2.4. Case D: uncertain reference data through applying noise signals

Measurements generally contain noise signals, which motivates us to study the case where Gaussian-distributed noise signals are induced onto the reference concentration field with zero mean and a standard deviation $\sigma \in \mathbb{R}$. The signal-to-noise ratio (SNR) quantifies the noise signal intensity, defined here as

$$\text{SNR} = \frac{\bar{c}_{\psi,\Omega_{\triangle x}}}{\sigma}, \tag{26}$$

where $\bar{c}_{\psi,\Omega}$ is the averaged concentration of a species over the whole numerical domain Ω before inducing noise signals. After computing the reference concentration field, the noise signal is applied grid-wise onto the reference data with the SNR, given by (26).

Fig. 16 illustrates the results for various SNRs for recovering one single reaction rate parameter, the reaction constant. This case required to include the reference concentration fields of all species ψ to reliably recover the reference parameters as in (16). In Fig. 16a, the reaction constant is recovered from the noisy reference data. The development of the relative error regarding the controls shows that decreasing SNR

results in an increase of the remaining relative error regarding the rate parameters. Fig. 16b illustrates the development of the minimized objective function over the performed simulations. Since the objective function in (16) gives the relative error between the reference solution and the current simulation, $J(\mathbf{c}(\boldsymbol{\alpha}^*), \boldsymbol{\alpha}^*)$ is equal to the error caused by the superposition of the noise signal onto the reference solution. This value of the relative error is indicated by solid lines in Fig. 16 for each tested noise intensity. The objective function aligns perfectly with the solid lines when the optimization algorithm terminates, indicating that the optimization algorithm successfully finds the minimal possible value of the objective function. Thus, the noise signal sets a lower limit regarding the objective function depending on the noise amplitude. By reaching that limit, the noise signal "blurs" the exact position of the local minima, leaving the gradient-based algorithm unable to get closer to the reference values. The optimization algorithm partially compensates for the induced error through noise signals by the control variables, i.e., the accuracy of the identified reaction rate parameters drops depending on the SNR. However, starting from a relative error of around 100% to the reference values, the parameter estimation framework reduces that error down to a magnitude lower than $< 1\%$ for an SNR of 5.

Fig. 17 presents the results obtained for $d_\alpha = 3$. Again, the reaction rate parameters can be recovered. Similar tendencies can be observed here, although the number of simulations increases compared to cases where no noise signals are induced. If prior estimations of $J(\boldsymbol{\alpha}^*)$ are available, the termination condition ϵ can be adjusted to reduce the number of simulations after reaching the lower threshold indicated by the solid lines in Fig. 17.
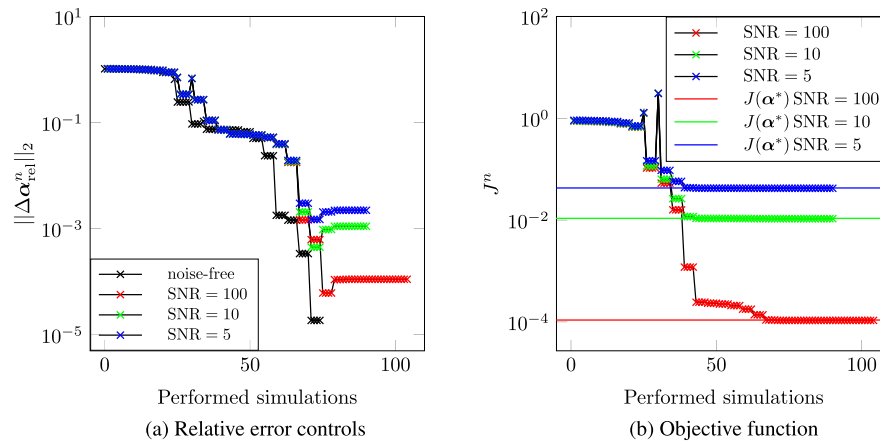
(a) Relative error controls

(b) Objective function

Fig. 17. Case D: Inducing uncertainty on the reference solution, compared for different noise intensities ($d_\alpha = 3$).
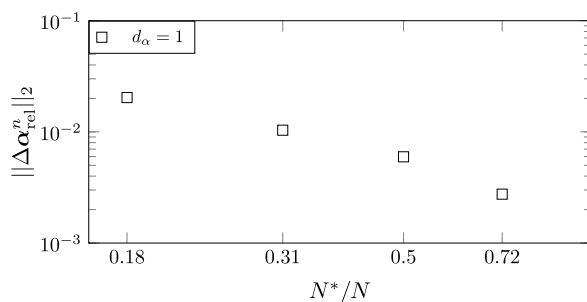

Fig. 18. Case E: The resolution of the reference simulation N^* is varied, whereby the resolution in the simulations during optimization N is fixed to $N = 96 \times 10^3$. The relative error regarding the reaction constant ($d_\alpha = 1$) is compared for various resolutions of $N^* < N$.

4.2.5. Case E: lower resolution in the reference simulation

In the final case, only the resolution of the reference simulation N^* is varied such that the resolution is lower than in those simulations performed during the optimization procedure, i.e., $N^* < N$. For the simulations during parameter estimation, the total resolution is set to the fixed number of $N = 96 \times 10^3$ cells. Further, reference concentration fields of all species are used in this case as in (16). The simulated concentration field $\mathbf{c}$ is interpolated onto the grid points of the reference simulation $\mathbf{x}^*$ to compute the objective function in (16). Fig. 18 shows the final relative error regarding the recovered reaction constant ($d_\alpha = 1$) for the tested reference simulation resolutions N^*. Here the decrease of the relative error can be observed for reducing the gap between the resolutions N and N^*. That is, the error between two successive simulations with decreasing grid spacing decreases as Fig. 6 ensures the grid convergence of the simulated flow problem. Therefore, by approaching N and N^* the discretization error as well as the interpolation error to compare $\mathbf{c}$ with $\mathbf{c}^*$ decrease and thus, the parameters can be recovered more accurately. Generally, we can not expect the objective function to become exactly zero for any set of reaction parameters, i.e., the reference and simulation distribution being identical. This can be due to various error sources, e.g., uncertainty in the measurement data, errors in the gradient computation, discretization, interpolation, and round-off errors, where their influence on the parameter identification is partially demonstrated in case D and E. The optimization problem compensates these error sources by adjusting the control parameters, which leads in an accuracy drop of the recovered parameters, see the results presented in Fig. 18 in comparison the results of case A. Note, that despite the poor resolution, the accuracy of the recovered parameters in Fig. 18 is still in an acceptable range, where the relative error is of the order $\mathcal{O}(1\%)$.

5. Conclusion

In this study, we investigated the feasibility of spatially distributed data for identifying reaction rate parameters in reactive flows using gradient-based PDE constrained optimization. Instead of solving the inverse problem by comparing reference data with simulated data at a single point or spatially averaged values, we minimized the error between a given reference and the simulated concentration field. The method was investigated for a generic homogeneous bulk reaction where a reference simulation with *a priori* known reaction rate parameters validated the implemented framework. Different configurations of the reference simulations were used to recover the reaction rate parameters while the presented method was analyzed regarding the accuracy of the parameters, the robustness of the approach, performance, and applicability on reduced or uncertain (noisy) reference data. The conclusions of this work are summarized below:

- Efficient, robust, and accurate identification of simultaneous identification of multiple parameters (Sec. 4.2.1 / Sec. 4.2.2)
- Reduction of the amount of accessible reference data; 1D data can be sufficient to recover parameters from a 2D flow field (Sec. 4.2.2 / Sec. 4.2.3)
- Applicability on uncertain (noisy) reference data; reduction of an initial relative error regarding the parameters from 100% down to 1% for a SNR of 5 (Sec. 4.2.4)
- Grid independence regarding optimization problem in the presented benchmark case (Sec. 4.2.1)
- Errors between reference and simulation, e.g., discretization error, noise signal, or interpolation error, are partially compensated by the identified parameters (Sec. 4.2.4 / Sec. 4.2.5)

This study presents a reliable and efficient method to identify reaction rate parameters from uncertain concentration distributions for the evaluated benchmark case involving a reactive flow. The next natural step would be the use of real MRI measurements, which involves remaining questions about the treatment of unknown boundary conditions, modeling errors due to simplified assumptions on the chosen reaction model, or other unavoidable errors due to the comparison between measurement and simulation to name a few. Despite those challenges, the remarkable advantages of the presented approach from the application-side perspective would be:

- Tests under ideal conditions will no longer have to be carried out to determine kinetic parameters
- The measurements can be made in the technical reactor using the original catalysts. (Of course, the latter must then be represented

Table 3
Present git contributions to unreleased OpenLB branches.

Keyword	Commit hash
EOC study	71332be411659dc73fe0687a25b0e6ac7ccda331
Cases A, B, C, D, and E	059944cc7312a13e2159810446ea44b0ea6f4bb8

in the simulation model in terms of pore size distribution and tortuosity.)

These benefits as well as the results of this work encourage the application of the presented method on real measurement data in future works.

CRediT authorship contribution statement

S.I.: Conceptualization, Methodology, Software, Validation, Formal analysis, Investigation, Data Curation, Writing – Original Draft. **J.J.:** Conceptualization, Formal analysis, Software, Writing – Review & Editing. **S.S.:** Formal analysis, Supervision, Software, Writing – Review & Editing. **F.B.:** Software, Writing – Review & Editing. **A.K.:** Software, Writing – Review & Editing. **A.Z.:** Writing – Review & Editing. **G.T.:** Writing – Review & Editing. **G.R.P.:** Conceptualization, Funding acquisition, Writing – Review & Editing. **J.T.:** Funding acquisition, Writing – Review & Editing. **M.J.K.:** Supervision, Conceptualization, Software, Resources, Funding acquisition, Writing – Review & Editing. All authors read and approved the manuscript.

Data availability

The numerical results in this work are produced with the open source C++ library OpenLB Release 1.6. Unreleased contributions are summarized with the corresponding commit hashes in Table 3. Datasets generated in this work are available from the authors upon reasonable request.

References

[1] H.F. Scott, Essentials of Chemical Reaction Engineering, second edition, International Series in the Physical and Chemical Engineering Sciences, Prentice Hall, [Place of publication not identified], 2017.

[2] M. Hettel, M. Wörner, O. Deutschmann, Computational fluid dynamics of catalytic reactors, in: W. Andreoni (Ed.), Handbook of Materials Modeling, Springer, Cham, 2018, pp. 1–34.

[3] R.C. Aster, B. Borchers, C.H. Thurber, Parameter Estimation and Inverse Problems, third edition, Elsevier, Amsterdam, Netherlands, 2019.

[4] B.M. Chaparro, S. Thuillier, L.F. Menezes, P.Y. Manach, J.V. Fernandes, Material parameters identification: gradient-based, genetic and hybrid optimization algorithms, Comput. Mater. Sci. 44 (2) (2008) 339–346, https://doi.org/10.1016/j.commatsci.2008.03.028, https://www.sciencedirect.com/science/article/pii/S0927025608001766.

[5] M. Ohsaki, B. Do, J. Fujiwara, T. Kimura, T. Yamashita, Two-step parameter identification of multi-axial cyclic constitutive law of structural steels from cyclic structural responses, Structures 46 (2022) 2014–2030, https://doi.org/10.1016/j.istruc.2022.11.007, https://www.sciencedirect.com/science/article/pii/S2352012422010463.

[6] D. Nolte, C. Bertoglio, Inverse problems in blood flow modeling: a review, Int. J. Numer. Methods Biomed. Eng. 38 (8) (2022) e3613, https://doi.org/10.1002/cnm.3613.

[7] M. Ismail, W.A. Wall, M.W. Gee, Adjoint-based inverse analysis of windkessel parameters for patient-specific vascular models, J. Comput. Phys. 244 (2013) 113–130, https://doi.org/10.1016/j.jcp.2012.10.028.

[8] L. Itu, P. Sharma, T. Passerini, A. Kamen, C. Suciu, D. Comaniciu, A parameter estimation framework for patient-specific hemodynamic computations, J. Comput. Phys. 281 (2015) 316–333, https://doi.org/10.1016/j.jcp.2014.10.034, https://www.sciencedirect.com/science/article/pii/S0021999114007165.

[9] P. Kügler, E. Gaubitzer, S. Müller, Parameter identification for chemical reaction systems using sparsity enforcing regularization: a case study for the chlorite-iodide reaction, J. Phys. Chem. A 113 (12) (2009) 2775–2785, https://doi.org/10.1021/jp808792u.

[10] A. Bermúdez, N. Esteban, J.L. Ferrín, J.F. Rodríguez-Calo, M.R. Sillero-Denamiel, Identification problem in plug-flow chemical reactors using the adjoint method, Comput. Chem. Eng. 98 (2017) 80–88, https://doi.org/10.1016/j.compchemeng.2016.11.029, https://www.sciencedirect.com/science/article/pii/S0098135416303775.

[11] Y. Ding, W. Zhang, L. Yu, K. Lu, The accuracy and efficiency of ga and pso optimization schemes on estimating reaction kinetic parameters of biomass pyrolysis, Energy 176 (2019) 582–588, https://doi.org/10.1016/j.energy.2019.04.030, https://www.sciencedirect.com/science/article/pii/S036054421930653X.

[12] Z. Till, T. Chován, T. Varga, Improved understanding of reaction kinetic identification problems using different nonlinear optimization algorithms, J. Taiwan Inst. Chem. Eng. 111 (2020) 73–79, https://doi.org/10.1016/j.jtice.2020.05.013, https://www.sciencedirect.com/science/article/pii/S1876107020301279.

[13] A. Al-Matouq, T. Vincent, A convex optimization framework for the identification of homogeneous reaction systems, Automatica 114 (2020) 108823, https://doi.org/10.1016/j.automatica.2020.108823, https://www.sciencedirect.com/science/article/pii/S0005109820300212.

[14] R. Trunk, T. Henn, W. Dörfler, H. Nirschl, M.J. Krause, Inertial dilute particulate fluid flow simulations with an Euler–Euler lattice Boltzmann method, J. Comput. Sci. 17 (2016) 438–445, https://doi.org/10.1016/j.jocs.2016.03.013, https://www.sciencedirect.com/science/article/pii/S1877750316300345.

[15] T. Henn, G. Thäter, W. Dörfler, H. Nirschl, M.J. Krause, Parallel dilute particulate flow simulations in the human nasal cavity, Comput. Fluids 124 (2016) 197–207, https://doi.org/10.1016/j.compfluid.2015.08.002, https://www.sciencedirect.com/science/article/pii/S0045793015002728.

[16] S. Simonis, M. Haussmann, L. Kronberg, W. Dörfler, M.J. Krause, Linear and brute force stability of orthogonal moment multiple-relaxation-time lattice Boltzmann methods applied to homogeneous isotropic turbulence, Philos. Trans. R. Soc. A, Math. Phys. Eng. Sci. 379 (2208) (2021) 20200405, https://doi.org/10.1098/rsta.2020.0405.

[17] S. Simonis, D. Oberle, M. Gaedtke, P. Jenny, M.J. Krause, Temporal large eddy simulation with lattice Boltzmann methods, J. Comput. Phys. 454 (2022) 110991, https://doi.org/10.1016/j.jcp.2022.110991, https://www.sciencedirect.com/science/article/pii/S0021999122000535.

[18] M. Haussmann, S. Simonis, H. Nirschl, M.J. Krause, Direct numerical simulation of decaying homogeneous isotropic turbulence — numerical experiments on stability, consistency and accuracy of distinct lattice Boltzmann methods, Int. J. Mod. Phys. C 30 (09) (2019) 1950074, https://doi.org/10.1142/S0129183119500748.

[19] M. Siodlaczek, M. Gaedtke, S. Simonis, M. Schweiker, N. Homma, M.J. Krause, Numerical evaluation of thermal comfort using a large eddy lattice Boltzmann method, Build. Environ. 192 (2021) 107618, https://doi.org/10.1016/j.buildenv.2021.107618, https://www.sciencedirect.com/science/article/pii/S0360132321000317.

[20] S.P. Sullivan, F.M. Sani, M.L. Johns, L.F. Gladden, Simulation of packed bed reactors using lattice Boltzmann methods, Chem. Eng. Sci. 60 (12) (2005) 3405–3418, https://doi.org/10.1016/j.ces.2005.01.038, https://www.sciencedirect.com/science/article/pii/S0009250905000916.

[21] Q.J. Kang, Peter C. Lichtner, David R. Janecky, Lattice Boltzmann method for reacting flows in porous media, Adv. Appl. Math. Mech. 2 (5) (2010) 545–563, https://doi.org/10.4208/aamm.10-10S02, https://www.researchgate.net/publication/257923166_Lattice_Boltzmann_Method_for_Reacting_Flows_in_Porous_Media.

[22] X. Meng, Z. Guo, Boundary scheme for linear heterogeneous surface reactions in the lattice Boltzmann method, Phys. Rev. E 94 (5–1) (2016) 053307, https://doi.org/10.1103/PhysRevE.94.053307.

[23] S.A. Hosseini, A. Eshghinejadfard, N. Darabiha, D. Thévenin, Weakly compressible lattice Boltzmann simulations of reacting flows with detailed thermo-chemical models, Comput. Math. Appl. 79 (1) (2020) 141–158, https://doi.org/10.1016/j.camwa.2017.08.045, https://www.sciencedirect.com/science/article/pii/S0898122117305473.

[24] D. Dapelo, S. Simonis, M.J. Krause, J. Bridgeman, Lattice-Boltzmann coupled models for advection–diffusion flow on a wide range of Péclet numbers, J. Comput. Sci. 51 (2021) 101363, https://doi.org/10.1016/j.jocs.2021.101363, https://www.sciencedirect.com/science/article/pii/S1877750321000557.

[25] S. Simonis, M. Frank, M.J. Krause, On relaxation systems and their relation to discrete velocity Boltzmann models for scalar advection-diffusion equations, Philos. Trans. R. Soc. A, Math. Phys. Eng. Sci. 378 (2175) (2020) 20190400, https://doi.org/10.1098/rsta.2019.0400.

[26] T. Krüger, H. Kusumaatmaja, A. Kuzmin, O. Shardt, G. Silva, E.M. Viggen, The Lattice Boltzmann Method: Principles and Practice, Graduate Texts in Physics, Springer International Publishing and Imprint and Springer, Cham, 2017.

[27] A. Kummerländer, M. Dorn, M. Frank, M.J. Krause, Implicit propagation of directly addressed grids in lattice Boltzmann methods, Concurr. Comput., Pract. Exp. 35 (8) (2023), https://doi.org/10.1002/cpe.7509.

[28] M.D. Gunzburger, Perspectives in Flow Control and Optimization, Advances in Design and Control, Society for Industrial and Applied Mathematics, Philadelphia, PA, 2003.

[29] D.C. Liu, J. Nocedal, On the limited memory bfgs method for large scale optimization, Math. Program. 45 (1–3) (1989) 503–528, https://doi.org/10.1007/BF01589116.

[30] F. Santosa, B. Weitz, An inverse problem in reaction kinetics, J. Math. Chem. 49 (8) (2011) 1507–1520, https://doi.org/10.1007/s10910-011-9835-2.

[31] K.R. Opara, P.P. Oh, Regularization and concave loss functions for estimation of chemical kinetic models, Appl. Soft Comput. 116 (2022) 108286, https://doi.org/10.1016/j.asoc.2021.108286, https://www.sciencedirect.com/science/article/pii/S1568494621010930.

[32] M.M. Britton, Mri of chemical reactions and processes, Prog. Nucl. Magn. Reson. Spectrosc. 101 (2017) 51–70, https://doi.org/10.1016/j.pnmrs.2017.03.001, https://www.sciencedirect.com/science/article/pii/S007965651730002X.

[33] F. Klemens, S. Schuhmann, G. Guthausen, G. Thäter, M.J. Krause, Cfd-mri: a coupled measurement and simulation approach for accurate fluid flow characterisation and domain identification, Comput. Fluids 166 (2018) 218–224, https://doi.org/10.1016/j.compfluid.2018.02.022.

[34] F. Klemens, B. Förster, M. Dorn, G. Thäter, M.J. Krause, Solving fluid flow domain identification problems with adjoint lattice Boltzmann methods, Comput. Math. Appl. 79 (1) (2020) 17–33, https://doi.org/10.1016/j.camwa.2018.07.010.

[35] F. Klemens, S. Schuhmann, R. Balbierer, G. Guthausen, H. Nirschl, G. Thäter, M.J. Krause, Noise reduction of flow mri measurements using a lattice Boltzmann based topology optimisation approach, Comput. Fluids 197 (2020) 104391, https://doi.org/10.1016/j.compfluid.2019.104391.

[36] F. Klemens, Combining computational fluid dynamics and magnetic resonance imaging data using lattice Boltzmann based topology optimisation, Ph.D. thesis https://doi.org/10.5445/IR/1000125499.

[37] J. Garay, D. Nolte, M. Löcke, C. Bertoglio, Parameter estimation in fluid flow models from aliased velocity measurements, Inverse Probl. 38 (9) (2022) 095002, https://doi.org/10.1088/1361-6420/ac836e.

[38] C.-H. Huang, C.-Y. Yeh, H.R. Orlande, A nonlinear inverse problem in simultaneously estimating the heat and mass production rates for a chemically reacting fluid, Chem. Eng. Sci. 58 (16) (2003) 3741–3752, https://doi.org/10.1016/S0009-2509(03)00270-7, https://www.sciencedirect.com/science/article/pii/S0009250903002707.

[39] A. Kummerländer, S. Avis, H. Kusumaatmaja, F. Bukreev, M. Crocoll, D. Dapelo, N. Hafen, S. Ito, J. Jeßberger, J.E. Marquardt, J. Mödl, T. Pertzel, F. Prinz, F. Raichle, M. Schecher, S. Simonis, D. Teutscher, M.J. Krause, Openlb release 1.6: open source lattice Boltzmann code, www.openlb.net/, 2023, https://doi.org/10.5281/ZENODO.7773497.

[40] M.J. Krause, A. Kummerländer, S.J. Avis, H. Kusumaatmaja, D. Dapelo, F. Klemens, M. Gaedtke, N. Hafen, A. Mink, R. Trunk, J.E. Marquardt, M.-L. Maier, M. Haussmann, S. Simonis, Openlb—open source lattice Boltzmann code, Comput. Math. Appl. 81 (2021) 258–288, https://doi.org/10.1016/j.camwa.2020.04.033.

[41] R.H. Byrd, P. Lu, J. Nocedal, C. Zhu, A limited memory algorithm for bound constrained optimization, SIAM J. Sci. Comput. 16 (5) (1995) 1190–1208, https://doi.org/10.1137/0916069.

[42] C. Geiger, C. Kanzow, Numerische Verfahren zur Lösung unrestringierter Optimierungsaufgaben, Springer-Verlag, 2013.

[43] Z. Guo, B. Shi, C. Zheng, A coupled lattice bgk model for the Boussinesq equations, Int. J. Numer. Methods Fluids 39 (4) (2002) 325–342, https://doi.org/10.1002/fld.337.

[44] Y.H. Qian, D. D'Humières, P. Lallemand, Lattice bgk models for Navier-Stokes equation, Europhys. Lett. 17 (6) (1992) 479–484, https://doi.org/10.1209/0295-5075/17/6/001.

[45] H. Yoshida, M. Nagaoka, Multiple-relaxation-time lattice Boltzmann model for the convection and anisotropic diffusion equation, J. Comput. Phys. 229 (20) (2010) 7774–7795, https://doi.org/10.1016/j.jcp.2010.06.037, https://www.sciencedirect.com/science/article/pii/S0021999110003529.

[46] P.L. Bhatnagar, E.P. Gross, M. Krook, A model for collision processes in gases. I. Small amplitude processes in charged and neutral one-component systems, Phys. Rev. 94 (3) (1954) 511–525, https://doi.org/10.1103/PhysRev.94.511.

[47] T. Seta, Implicit temperature-correction-based immersed-boundary thermal lattice Boltzmann method for the simulation of natural convection, Phys. Rev. E, Stat. Nonlinear Soft Matter Phys. 87 (6) (2013) 063304, https://doi.org/10.1103/PhysRevE.87.063304.

[48] G. Gruszczyński, M. Dzikowski, Ł. Łaniewski-Wołłk, Revisiting the second-order convergence of the lattice Boltzmann method with reaction-type source terms, Comput. Math. Appl. 144 (2023) 34–50, https://doi.org/10.1016/j.camwa.2023.05.020, https://www.sciencedirect.com/science/article/pii/S0898122123002237.

[49] J. Jeßberger, J.E. Marquardt, L. Heim, J. Mangold, F. Bukreev, M.J. Krause, Optimization of a micromixer with automatic differentiation, Fluids 7 (5) (2022) 144, https://doi.org/10.3390/fluids7050144.

[50] A. Griewank, Evaluating Derivatives: Principles and Techniques of Algorithmic Differentiation, 2nd edition, SIAM, Philadelphia, PA, 2008.

[51] R. Allen, T. Reis, Moment-based boundary conditions for lattice Boltzmann simulations of natural convection in cavities, Prog. Comput. Fluid Dyn. 16 (4) (2016) 216, https://doi.org/10.1504/PCFD.2016.077296, https://www.researchgate.net/publication/296194443_Moment-based_boundary_conditions_for_lattice_Boltzmann_simulations_of_natural_convection_in_cavities.